1993SoPh..146..207C

ON THE CALIBRATION OF LINE-OF-SIGHT MAGNETOGRAMS

G. CAUZZI*
Departimento di Astronomia e Fisica della Spazio, University of Florence, 50125 Firenze, Italy
L. A. SMALDONE*
Dipartimento di Science Fisiche, University of Naples, Mostra d'Oltremare, 80125 Napoli, Italy
K. S. BALASUBRAMANIAM**
*National Solar Observatory/Sacramento Peak, National Optical Astronomical Observatories***, Sunspot, NM 88349, U.S.A.*
and
S. L. KEIL
Phillips Laboratory (AFMC), Geophysics Directorate, USAF, National Solar Observatory/Sacramento Peak, Sunspot, NM 88349, U.S.A.

(Received 23 November, 1992; in revised form 5 February, 1993)

Abstract. Inference of magnetic fields from very high spatial, spectral, and temporal resolution polarized images is critical in understanding the physical processes that form and evolve fine scale structures in the solar atmosphere. Studying high spectral resolution data also helps in understanding the limits of lower resolution spectral data. We compare three different methods for calibrating the line-of-sight component of the magnetic field. Each method is tested for varying degrees of spectral resolution on both synthetic line profiles computed for known magnetic fields and real data. The methods evaluated are: (a) the differences in the center of gravity of the right and left circular components for different spectral resolution, (b) conversion of circular polarization, at particular wavelengths, to magnetic fields using model-dependent numerical solutions to the equations of polarized radiative transfer, and (c) the derivative method using the weak field approximation. Each method is applied to very high spatial and spectral resolution circular polarization images of an active region, acquired in the Fe I 5250 Å Zeeman-sensitive spectral line. The images were obtained using the 20 mÅ pass-band tunable filter at NSO/Sacramento Peak Observatory Vacuum Tower Telescope. We find that the center-of-gravity separation offers the best way of inferring the longitudinal magnetic field.

1. Introduction

Magnetic fields in the solar atmosphere have the remarkable ability to arrange themselves spatially into features ranging in size from large active regions (several arc min) down to small flux tubes (<0.3 arc sec). The strength of the magnetic field and the magnetic flux associated with these features play a crucial role in determining their characteristics and evolutionary properties. The concentration

---

* Work partially done while the author held an NRC-USAF Resarch Associateship.

** Supported under a USAF/AFOSR research initiative.

*** The National Optical Astronomy Observatories are operated by the Association of Universities Research in Astronomy, Inc. (AURA), under cooperative agreement with the National Science Foundation (NSF). Partial support for National Solar Observatory is provided by the United States Air Force under a Memorandum of Understanding with NSF.

Solar Physics **146:** 207–227, 1993.

of field into flux tubes and its interaction with flow fields is now recognized as the primary ingredient in atmospheric heating, flares, mass ejections, high speed solar wind streams, and energetic particle acceleration. Many of the processes responsible for field evolution occur on subarcsecond scales, and distinguishing among them requires observations at very high spatial resolution. We must measure the field strength as well as the motions at these subarcsecond scales in order to make progress in modeling of the processes. To this end, a very narrow spectral bandpass filter system has been developed for use in high spectral and spatial resolution observations of the solar atmosphere (this system is described in Bonaccini and Stauffer, 1990; and Cauzzi, 1992).

When used to measure magnetic field, the filter is stepped through a Zeeman-sensitive line in both states of circularly polarized light. Accurate conversion of the polarization images to magnetic field measurements will play a crucial role in developing an understanding of the role magnetic field plays in the Sun. Whether the fields dominate or whether the atmospheric dynamics do, depends on the actual strength and orientation of the field. Errors in determining the field can result in an incorrect assessment of the physical processes in the atmosphere.

In addition to obtaining good quality observations, which in itself is a challenging problem, we must take extreme care in calibrating the polarization signals. Several methods for converting polarization measurements into solar magnetic fields have been discussed in the literature. These methods vary, depending on the type of instrument used to measure the polarization and the application of the field measurements. Instrumentation falls into two broad categories, full line spectromagnetographs, which have high spectral resolution, but must be spatially scanned to obtain a two-dimensional solar image (Lites *et al.*, 1991; Jones *et al*;, 1992; Mickey, 1985), and imaging, filter magnetographs with continuous spatial coverage, but poor spectral resolution (Hagyard *et al.*, 1982; Zirin, 1985; Ai, 1987; Makita, Hamana, and Nishi, 1985; Rust and O'Byrne, 1991; Lundstedt *et al.*, 1991; Title, Tarbell, and Topka, 1987). The advent of narrow-band filter systems holds out the promise of combining the best features of both categories.

Calibration methods for line-of-sight magnetograms include (a) wavelength separation of the center of gravity of the sigma components proportional to the magnetic field (Rees and Semel, 1979), (b) conversion of the observed polarization at a given wavelength in the spectral line, using model-dependent polarized radiative transfer calculations to derive the magnetic field (Hagyard, Gary, and West, 1988), and (c) conversion of the observed polarization at a particular wavelength in the line, using the derivative of the intensity profile in the weak field approximation (Landi Degl'Innocenti and Landi Del'Innocenti, 1973; Jefferies and Mickey, 1991).

This paper examines the influence of the calibration process in the determination of line-of-sight magnetograms, using a narrow-band imaging system. The major advantage of using a narrow-band system stems from its ability to step through the line and measure a complete line profile. Although the points in the line are not obtained simultaneously, and are thus subject to errors due to image motion, image blurring, and evolution of solar features, modern image stabilization, destreching routines and high-speed CCD detectors permit us to partially compensate for these problems. The common practice with filter magnetographs is to observe left and right circularly polarized light at only one or two wavelengths. This decreases the time needed to make a magnetogram giving better temporal resolution and decreases the problems related to seeing changes, but it can lead to significant error in the determination of field strengths and orientation. Using the tunable, narrow-band filter, it is possible to compare various methods of obtaining longitudinal magnetic field measurements from a filter system. By comparing the various methods, our goal is to verify the inherent limitations of each one of them, applied to the same data set of high spatial and spectral resolution.

Since the actual magnetic field on the Sun is unknown, we cannot directly compare the different calibration methods by deriving the solar field from the observational data. We would not know which method yields a result closest to the actual solar field. Hence, in Section 2, we establish a basis to examine the influence of each of these calibration methods on synthetic line profiles with known magnetic fields. Section 3 describes the instruments used in the data collection and Section 4 describes the application of th emethods to real data. A comparative analysis of the simulated calibration and the real data calibration is described in Section 5. A summary of the analysis and the resulting implications are discussed in Section 6.

The Fe I 5250.2 Å spectral line (Landé $g = 3.0$) has been a familiar spectral line used in the measurement of magnetic fields. We have used this spectral line in our simulations as well as in the observations. It is worthwhile to note that we have assumed that the magnetic field observed in each resolution element completely fills the resolution element, and hence the magnetic filling factor is unity, even though this is rarely realized in practice. However, this assumption should not affect the results since the methods compare magnetic flux, and the filling factor affects all these methods in the same way.

2. Calibration of the Longitudinal Magnetic Field – Simulations

In order to test the calibration methods, we synthesized spectral line profiles for various atmospheric models, with known magnetic field strengths, and then attempted to recover the input field strengths using each one of the methods. Factors like width of the instrumental profiles, model dependence, velocity effects have been taken into account in the recovery process.

Stokes' profiles for the Fe I 5250.2 Å line were numerically simultaed from the equation of polarized radiative transfer, using the MALIP code of Landi Degl'Innocenti (1976). These calculations have been performed under the restrictive assumptions of Local Thermodynamic Equilibrium (LTE). The magnetic field strength and its inclination are assumed to be a constant, within the depth of formation of the spectral line. Calculations were made for the HSRA photosphere (Gingerich *et al.*, 1971) and the penumbral model of Kjeldseth-Moe and Maltby (1969, hereafter referred to as KM) using a grid of magnetic field values ranging from 0 to 2500 G, in steps of 50 G, and for magnetic field inclinations, (θ), of 0°, 30°, and 60°. We have avoided using umbral models in these calculations, as they lack continuity with the penumbral models.

The synthetic line profiles have been convolved with three different instrumental profiles: (i) an Airy function of 20 mÅ full-width at half-maximum (FWHM), representing the spectral transmission profile of the narrow-band filter at the NSO/Sacramento Peak Vacuum Tower Telescope, (ii) a Gaussian function of 60 mÅ FWHM, approximating the spectral smearing characteristics of the SOUP filter (Title, Tarbell, and Topka, 1987), and (iii) a Gaussian function of 120 mÅ FWHM, approximating the spectral smearing characteristics of the NASA Marshall Space Flight Center Vector Magnetograph (Hagyard *et al.*, 1982).

2.1. THE CENTER-OF-GRAVITY METHOD

The center-of-gravity separation of the circularly polarized σ-components ($I_\pm$) has log been used to measure the longitudinal magnetic field. The center of gravity of the $I_\pm$ profiles is defined as

$$\lambda_\pm = \frac{\int (I_c - I_\pm(\lambda))\lambda \, \mathrm{d}\lambda}{\int (I_c - I_\pm(\lambda)) \, \mathrm{d}\lambda} \,, \tag{1}$$

where I_c is the continuum intensity for the right or left circular polarization components.

The longitudinal component of the magnetic field, $B_{||}$, is estimated by (Rees and Semel, 1979)

$$B_{||} = \frac{(\lambda_+ - \lambda_-)/2.0}{4.667 \times 10^{-13} \lambda_0^2 g_\mathrm{L}} \,, \tag{2}$$

where λ_0 is the central wavelength of the spectral line and g_L is the Landé splitting factor ($B_{||}$ given in gauss and the wavelengths in Å). According to Rees and Semel, this formula can be used to derive the value of $B_{||}$ with an accuracy of ~10% for any inclination of the magnetic field vector.

We have applied the center-of-gravity method to the simulated right and left circular component profiles and derived the line-of-sight component of the magnetic field. Figure 1 summarizes the results we obtained for the KM-penumbral model, where the synthetic profiles have been convolved with the instrumental profiles, cited above. Our results confirm the statements of Rees and Semel (1979). The center-of-gravity method gives an estimate of $B_{||}$ to within an error of ~12% when the magnetic field is increased to 2500 G. We also found that this recovery had almost no dependence on the width of the instrumental profile.

When dealing with real data, unfortunately, the presence of blends restricts the useful spectral interval for the line of interest, and limits the accuracy of the

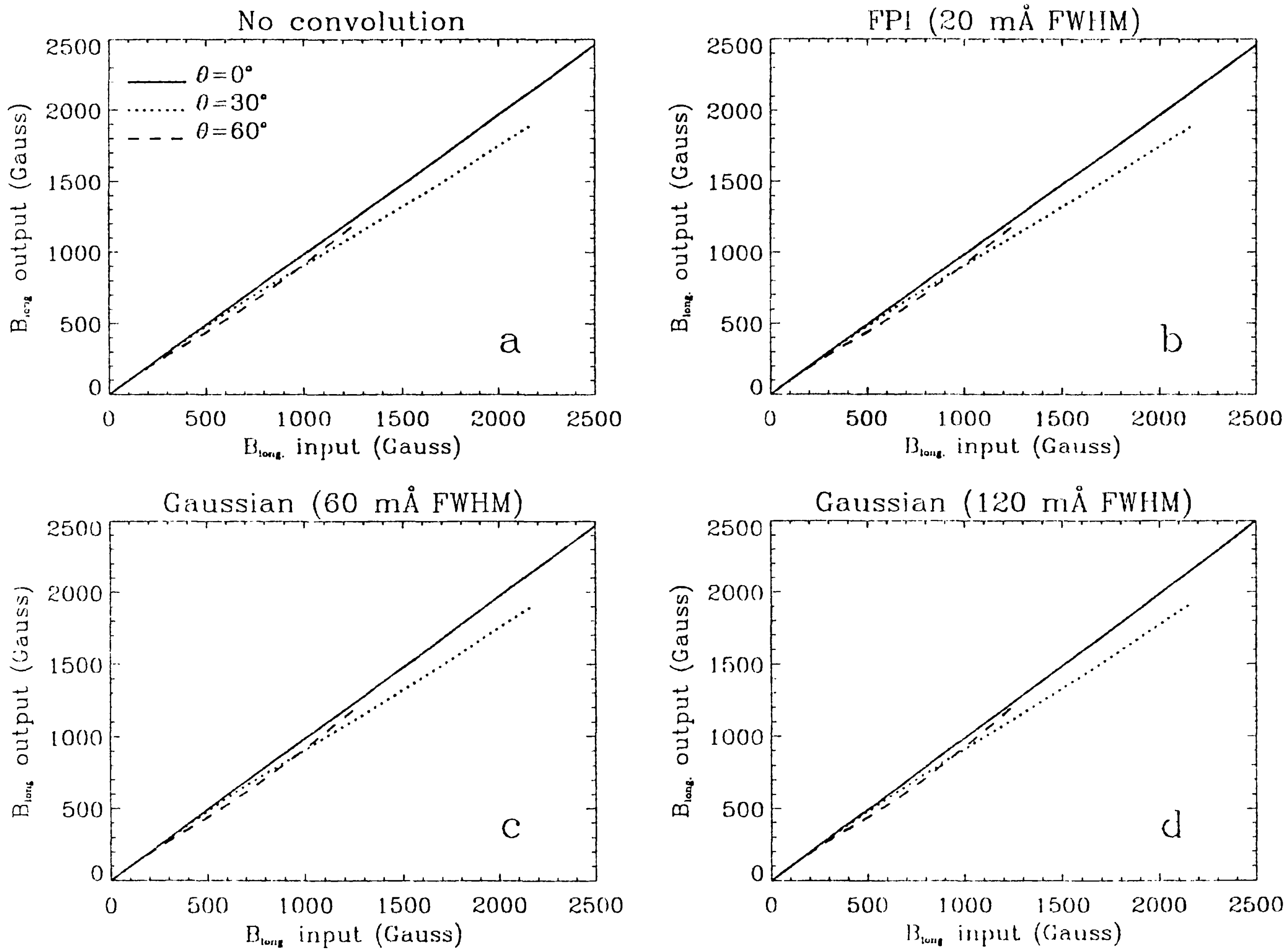

Fig. 1. The center-of-gravity method using synthetic profiles. Each of these curves is a comparison of the recovered magnetic field versus the known input magnetic field, where the KM-penumbral model was used to compute the line profiles. The solid, dotted, and dashed curves represent inclinations of the fields, with respect to the line of sight (θ) of 0°, 30°, and 60°, respectively. Shown here are the recovered magnetic fields for the spectral lines with (a) infinite resolution, (b) through a Fabry–Pérot filter with 20 mÅ FWHM, (c) through a filter with a 60 mÅ FWHM Gaussian profile, and (d) through a filter with a 120 mÅ FWHM Gaussian profile.

center-of-gravity method. For the Fe I 5250.2 Å, the lines Fe I 5250.6 Å on the red side and Co 5250.04 Å on the blue side restrict the usable spectral range to $\lambda_0 \pm 140$ mÅ. Fe I 5260.6 Å is also magnetically sensitive ($g_L = 1.16$) and can introduce spurious errors in the case of strong magnetic fields (Kjeldseth-Moe, 1973; Balasubramaniam, 1991).

The effects of restricting the spectral range to avoid blends, on the determination of $B_{||}$ have been evaluated by applying Equations (1) and (2) to the synthetic profiles, limited to the interval $\lambda_0 \pm 120$ mÅ. This has been done to facilitate comparison with the observed data shown in Section 3. The results are shown in Figure 2. The magnetic field is systematically underestimated. The amplitude of this underestimation increases with the width of the instrumental profile because

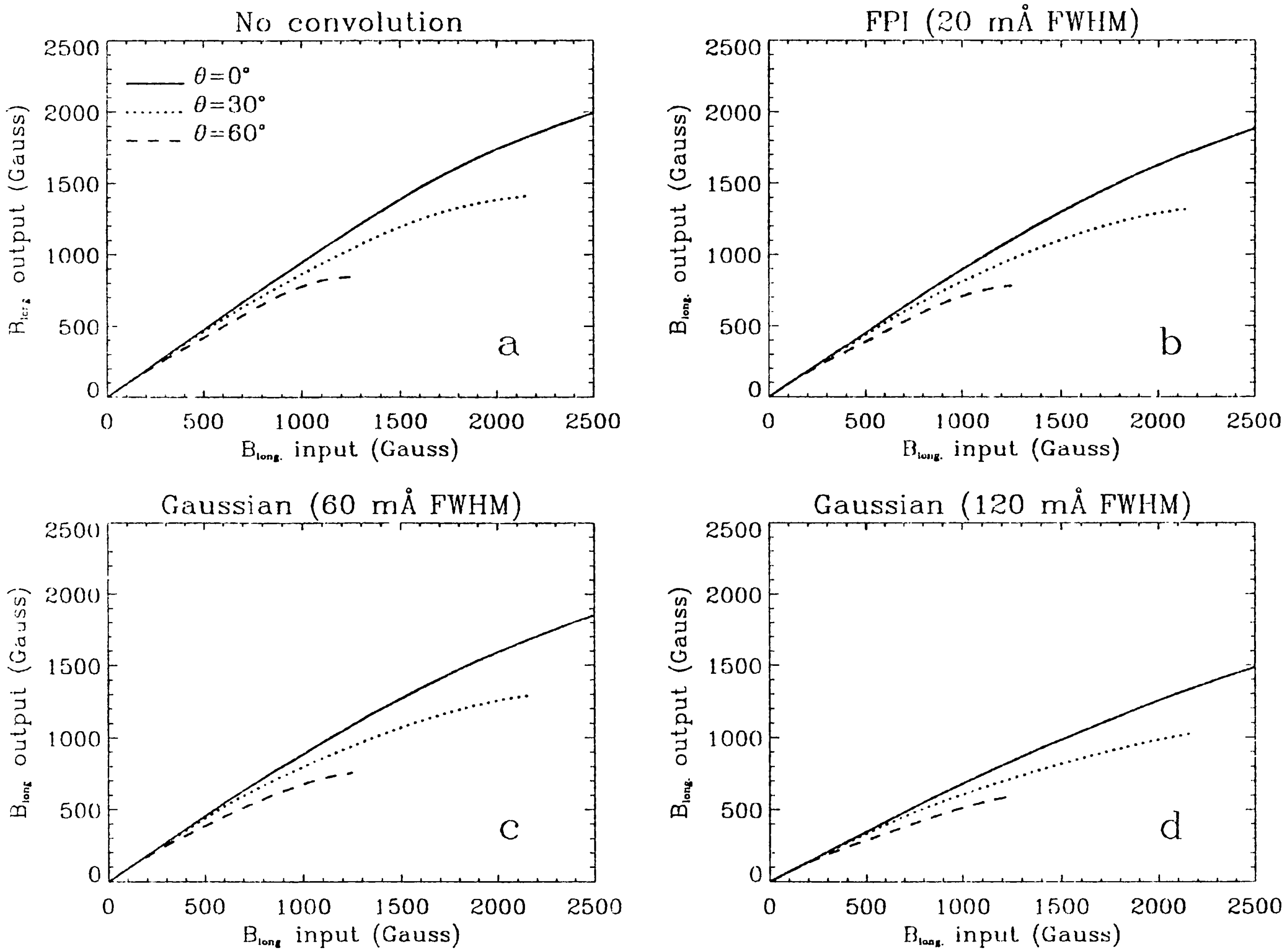

Fig. 2. The center-of-gravity method using synthetic profiles with restricted sampling. Each of these curves is similar to the ones shown in Figure 1. These curves were derived using a sampling restricted to ±120 mÅ on either side of the line center, in an effort to avoid blends.

the signal is 'redistributed' more into the wings by the smearing of the broader instrumental profile. This error can reach ~30% even for the narrowest instrumental profile, for large fields at high inclinations. This factor is important for comparing the different calibration methods, as will be done in Section 4.

2.2. CALIBRATION AT SINGLE WAVELENGTH THROUGH MODELING

Many filter magnetographs measure the circular polarization at a single wavelength in the outer wings of a spectral line, where the polarization signal is still discernible. The wings were chosen because magneto-optic effects influence the measurements closer to the spectral line center (Wittmann, 1971; Landi Degl'Innocenti, 1979). Calibration curves derived from model-dependent calculations, using polarized radiative transfer, are then used to convert the observed polarization at the single wavelength to longitudinal magnetic fields. The MSFC Vector Magnetograph (Hagyard *et al.*, 1982) is a representative example of this class of instruments.

For the Fe I 5250.2 Å line, we derived the fractional circular polarization signal,

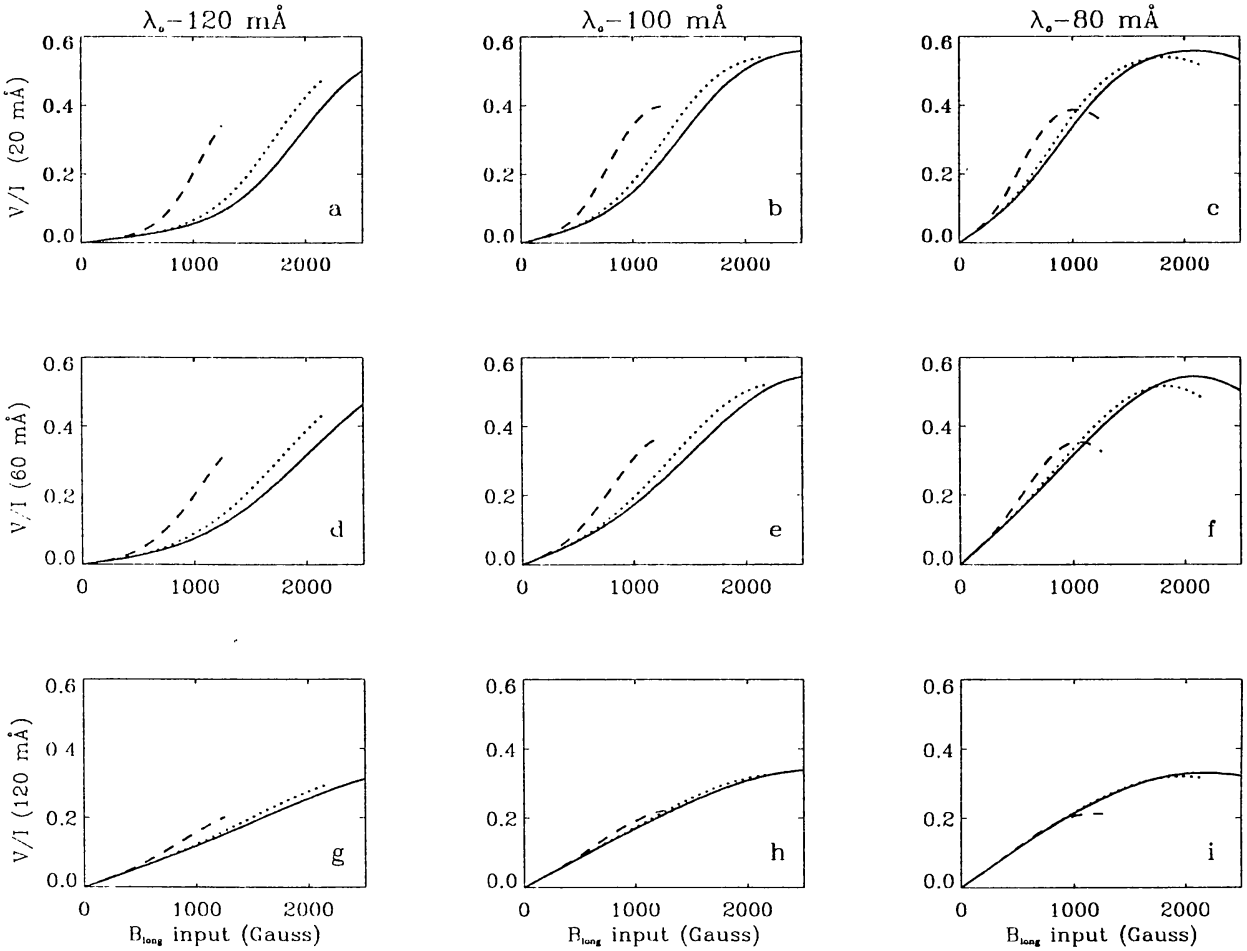

Fig. 3a–i. Single-wavelength calibration method used to recover the longitudinal magnetic field. Figures represent the calibration curves used to derive the magnetic field, for a given value of the fractional polarization, V/I, using the KM-penumbral model. Horizontal rows (top to bottom) represent the calibration curves for different spectral resolutions Vertical columns represent the locations in the blue wings of the spectral line (−120 mÅ, −100 mÅ, and −80 mÅ). The solid, dotted, and dashed curves represent inclinations of 0°, 30°, and 60°, respectively.

V/I, as a function of the longitudinal magnetic field strength, for different wavelengths and field inclinations. The curves, V/I versus $B_{\|}$ for the penumbral model are shown in Figure 3 for three different wavelengths in the blue wing (λ − 120, −100, −80 mÅ) and the three instrumental profiles. The blue wing was chosen because it is not contaminated by blends. The HSRA model gives essentially the same curves, but with lower polarization values.

In planning the observations, one must take into account the following constraints, clearly emerging from Figure 3:

(a) for any spectral resolution, the saturation of the polarization signal shifts to stronger values of the field further out in the wings; at the same time the signal for small fields (say, $B_{\|} \leq 500$ G) gets correspondingly much smaller. The optimum wavelength for measuring the polarization, therefore, depends on the magnetic features one plans to observe.

(b) At any given spectral position, the saturation values depend on the inclination of the magnetic field. Curves computed for different values of θ vary significantly as we obtain measurements further into the wings of the spectral line (Figures 3(a), 3(b), 3(d), 3(e)).

(c) With increasing width of the instrumental profile, the fractional polarization becomes smaller, but its variation with the input magnetic field tends to be linear. Hence, given the wavelength of observation and the instrument profile, we need to know the atmospheric model and the inclination of the fields to arrive at typical calibration curves. The above results suggest that the best combination of spectral positions and spectral smearing functions for comparing synthetic line profiles with real data are: (a) at -80 mÅ, for the 20 mÅ FPI (Figure 3(c)), (b) at -80 mÅ, for the 60 mÅ Gaussian profile (Figure 3(f)), and (c) at -100 mÅ, for the 120 mÅ Gaussian profile (Figure 3(h). Each of these cases is considered for an inclination of $\theta = 30°$.

Errors in the recovered magnetic field using this method are usually due to an incorrect choice of the atmospheric model (cf. Stenflo, 1989). Although different features can be present within the observed field of view (FOV) (penumbra, pores, photosphere, filigree, etc.) and each of them should, in principle, be presented by an independent model, this may not be possible under some circumstances. For example, it is not always a straightforward task to uniquely identify the different features in the FOV, given observations obtained in a few wavelengths of a single spectral line (see Figure 8).

To estimate the errors due to model dependence, we applied the KM-penumbral calibration curve to the photospheric polarization signal and $vice\ versa$, for each spectral resolution. These results are shown in Figure 4, for the profiles convolved with the 120 mÅ Gaussian. Other smearing functions essentially follow the same pattern. There is an underestimate of $B_{||}$ when applying the penumbral calibration curves to the photospheric signal and $vice\ versa$, the errors are about 30%.

Other errors, generally neglected, which could be relevant in the determination of $B_{||}$, result from the line-of-sight velocity fields. The velocity effect equates to tuning the filter to different wavelengths. Any filter magnetograph measures the polarization signal at a $fixed$ wavelength, $\Delta\lambda$, away from line center for a given FOV, while a Doppler shift of the spectral line within the FOV alters the signal. Since the conversion of the V/I signal into $B_{||}$ values is done with calibration curves valid for the $fixed$ wavelength, the final effect of a Doppler shift will be a net underestimate or overestimate of the field, depending on the direction of the shift and the position in the linewings. Figure 5 shows the errors introduced by a line-of-sight velocity of ± 0.5 and ± 1 km s^{-1} for each of the three spectral resolutions (the corresponding wavelength shift is $\sim$10 and 20 mÅ, respectively; this last value of velocity can be regarded as an upper limit in most of the photospheric cases). Even a modest velocity field (or an equivalent error in the tuning of the filter) introduces errors up to a few hundred gauss, and can lead to a wrong determination of $B_{||}$, especially for small fields. The situation improves with increasing width of the

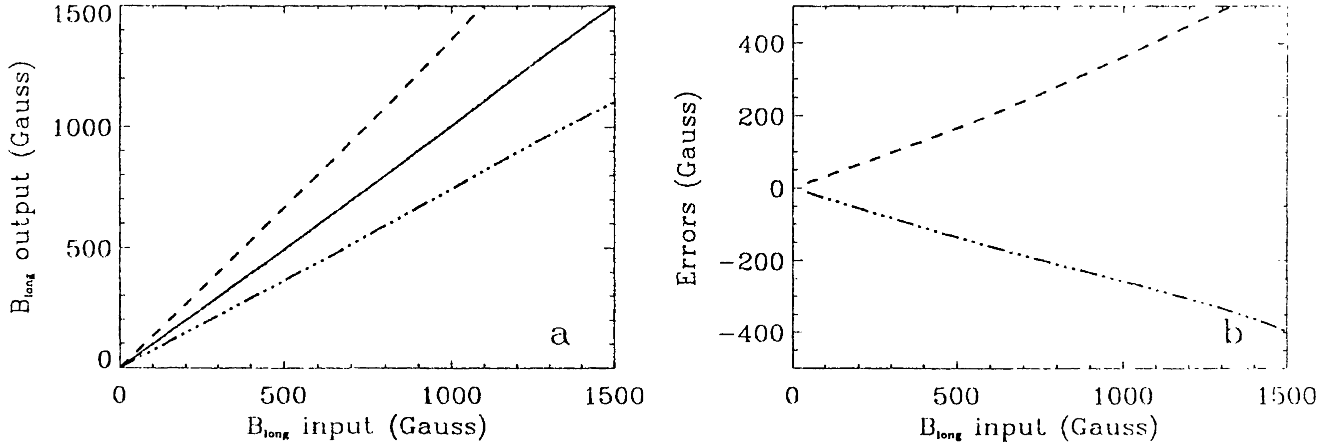

Fig. 4. Magnetic fields recovered from single-wavelength calibration curves, compared with the input magnetic fields, and errors resulting from this comparison. (a) Dashed curves represent the magnetic fields from a penumbral polarization signal recovered using the photospheric model, dot-dashed curves represent the magnetic fields from a photospheric polarization signal calibrated using the penumbral model. The solid line represents the one-to-one correspondence between the input and the recovered fields. (b) Errors resulting from the two calibrations, as a function of the input magnetic fields, as shown in (a). Using the wrong atmospheric model will result in an incorrect assessment of the magnetic fields.

instrumental profiles (Figures 5(c), 5(f)), but still the errors can be a significant fraction of the input $B_{||}$ values. Hence, velocity fields represent a serious problem for the calibration at one single wavelength, and for observations at high spectral resolution (FWHM$\leq 2\Delta\lambda_D$).

The last source of error we have investigated is due to the inclination of the magnetic field on the Sun. The calibration curves are computed for fields with a given inclination, however nothing is known *a priori* about the true inclination. We computed the calibration curve for fields having an inclination of 30° and applied this calibration curve to translate the V/I signal, for inclinations of 0°, 30°, and 60°, to $B_{||}$ values. The corresponding errors are shown in Figure 6 for the KM-penumbral model. Again, the errors are larger for the higher spectral resolutions, and there is also no significant difference of behavior for the two atmospheric models. The errors due to inclination are, however, much lower than errors due to velocity fields.

2.3. DERIVATIVE METHOD IN THE WEAK FIELD APPROXIMATION

The weak field approximation (WFA) is usually defined as the regime where the Zeeman splitting is much smaller than the Doppler width, $\Delta\lambda_D$, of the line. (For Fe I 5250.2 Å, assuming a Doppler width of ~40 mÅ, this translates into a magnetic field of $\ll$1000 G.) In the weak field approximation the transfer equations for Stokes' parameters simplify greatly, and, for the case of longitudinal magnetic field and a normal Zeeman triplet, we can write (Landi Degl'Innocenti and Landi Degl'Innocenti, 1973)

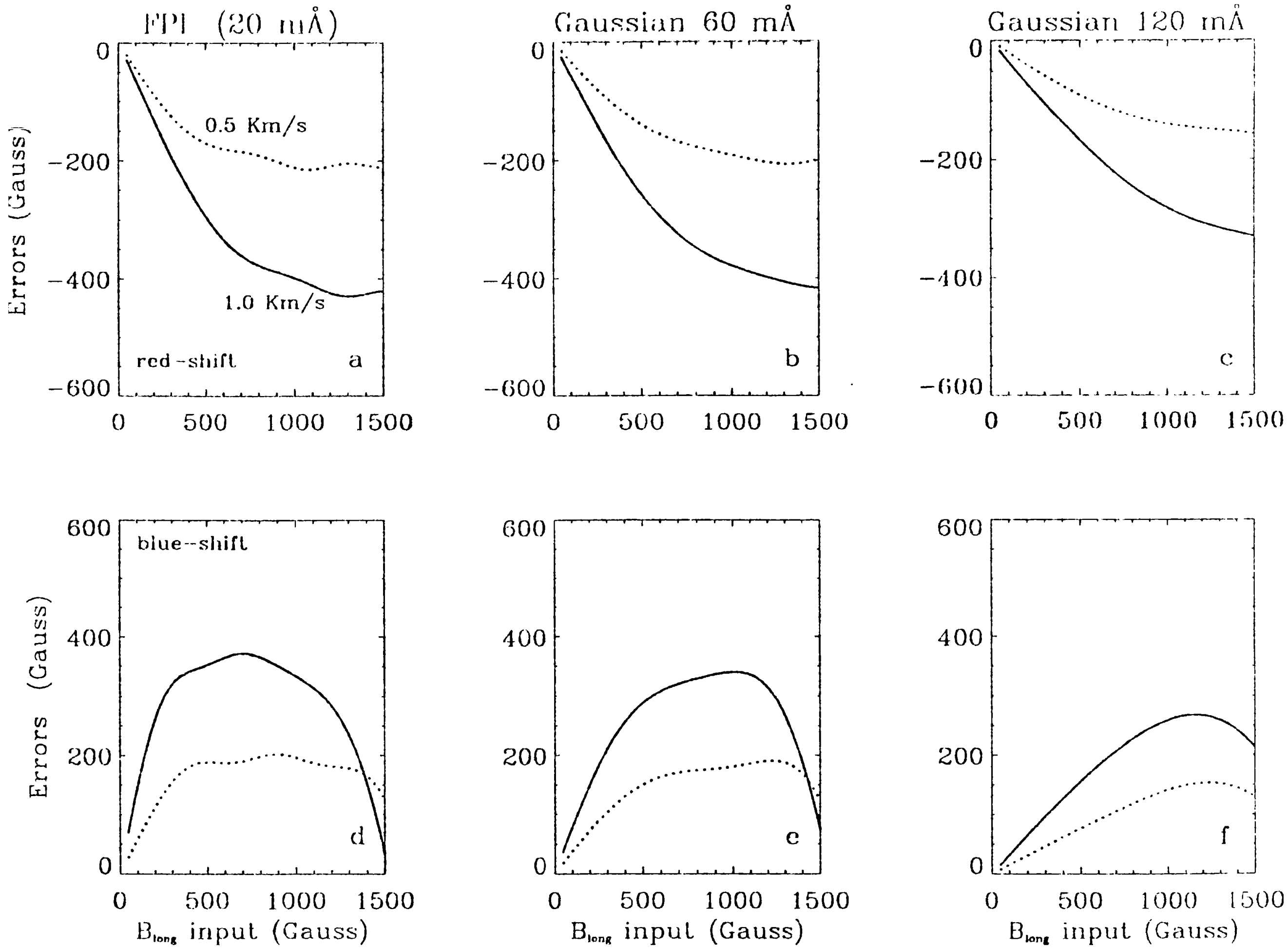

Fig. 5. Errors due to velocity effects using the single wavelength calibrations, in the blue wing of the spectral line, using the penumbral model. Left and middle columns are the errors determined at −80 mÅ, and the right column are the errors at −100 mÅ; the spectral smearing considered in each case is indicated on the top of each column. The errors are shown as a function of the input magnetic field. Dotted lines are for a velocity of 0.5 km s^{-1}, and the solid lines are for a velocity of 1.0 km s^{-1}. The top row represents the errors due to a red-shift and the bottom row represents the errors due to a blue shift. The top and bottom rows would qualitatively interchange, if one were to observe in the red wings of the spectral line.

$$V = -\mu \lambda_0^2 g_{\mathrm{L}} B_{\|} \frac{\mathrm{d}I_0}{\mathrm{d}\lambda} \,, \tag{3}$$

where μ is the Bohr magneton, g_{L} the Landé factor, λ_0 the line-center wavelength, and I_0 the Stokes intensity profile obtained in the absence of magnetic field.

In Section 2.2, the constant of proportionality between $B_{\|}$ and Stokes' V was obtained using models. However, using Equation (3), we could estimate $B_{\|}$ directly from V by measuring $\mathrm{d}I/\mathrm{d}\lambda$. In the case of a filter magnetograph, $\mathrm{d}I/\mathrm{d}\lambda$ can be obtained observing at a couple of wavelengths in the wing of the line. Both the weak field approximation and the fact that what we measure is the actual I profile (affected by the presence of magnetic field) instead of a non-magnetic I_0, restricts the range of validity of Equation (3).

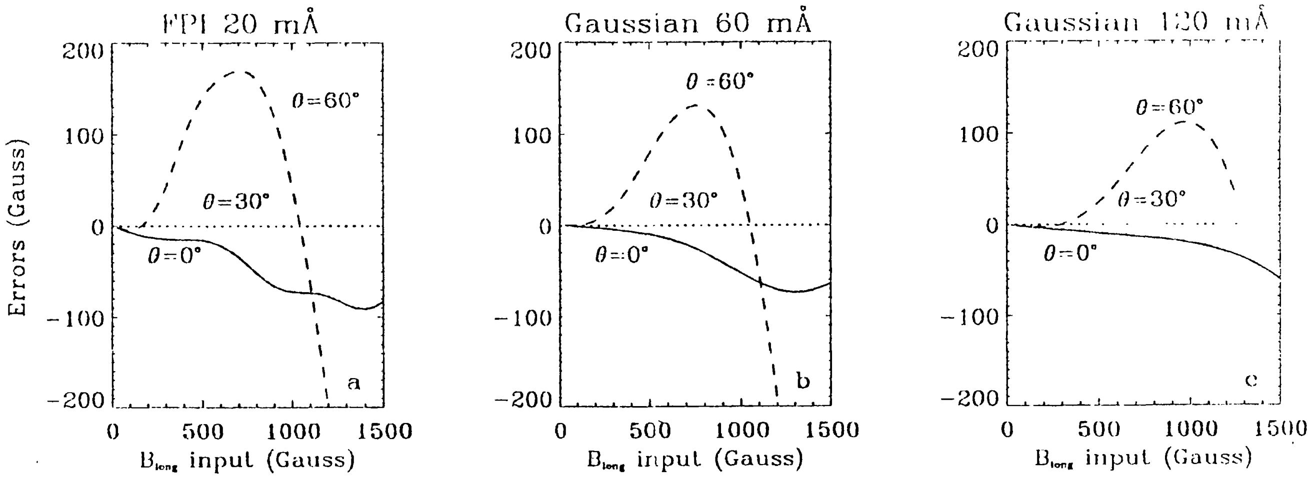

Fig. 6. Errors in the recovered magnetic field, due to inclination effects, using the single-wavelength calibration, for a penumbral model. The curves are shown using a single calibration curve having an inclination of 30°, for the three spectral smearing cases, respectively. The wavelengths used in these calibration curves are the same as in Figure 5. In the simulations, the input inclinations are known, hence the errors are shown separately for the input inclinations of 0°, 30°, and 60°.

In a recent paper, Jefferies and Mickey (1991, hereafter referred as JM), carefully investigated the errors related to the use of Equation (3) and concluded that its range of validity can be extended up to $\mathbf{B} \simeq 3500/g_{\mathrm{L}}$ G (for a spectral line at 6000 Å), provided that we observe far in the line wings, i.e., beyond $\sim 3\Delta_D$ from line center. Following JM, Equation (3) will result in a maximum error of 20% for field strengths up to 1500 G, for the Fe I 5250.2 Å line. This error is independent of any atmospheric model and has a low sensitivity to velocity effects.

The derived values of $B_{\|}$ obtained using Equation (3), in units of the input value of the magnetic field, are shown in Figure 7(a), as a function of the position in the wings and for several values of the field (**B**=100, 500, 1000, and 1500 G; $\theta = 0°$). Beyond 120 mÅ from the line center, the WFA works well for the Fe I 5250.2 Å line when $\mathbf{B} \leq 500$ G. At higher values of the field, the curves never reach unity and the error gets small only near 200 mÅ from the line center. However, at these wavelengths the small polarization signal (<0.3% of the intensity value, for a field of 1000 G) and the presence of blends invalidates use of Equation (3).

We have studied the influence of spectral smearing on the recovered fields using the derivative method, in the WFA. Figures 7(b–d) show the curves of Figure 7(a), after Stokes' parameters have been convolved with the three instrumental profiles. The net effect of a wider instrumental profile is the 'smoothing' of the curves, and their flattening around the unity value. There exists a curious situation, as depicted in Figure 7(d) (Gaussian profile of 120 mÅ FWHM) where the estimate given by Equation (3) holds reasonably well from ~80 mÅ to 150 mÅ from line center, even for strong values of the magnetic field, but not further out in the wings.

This calibration method is suitable for line-of-sight filter magnetographs, up to the numerical limits established by JM, but needs careful preliminary analysis in

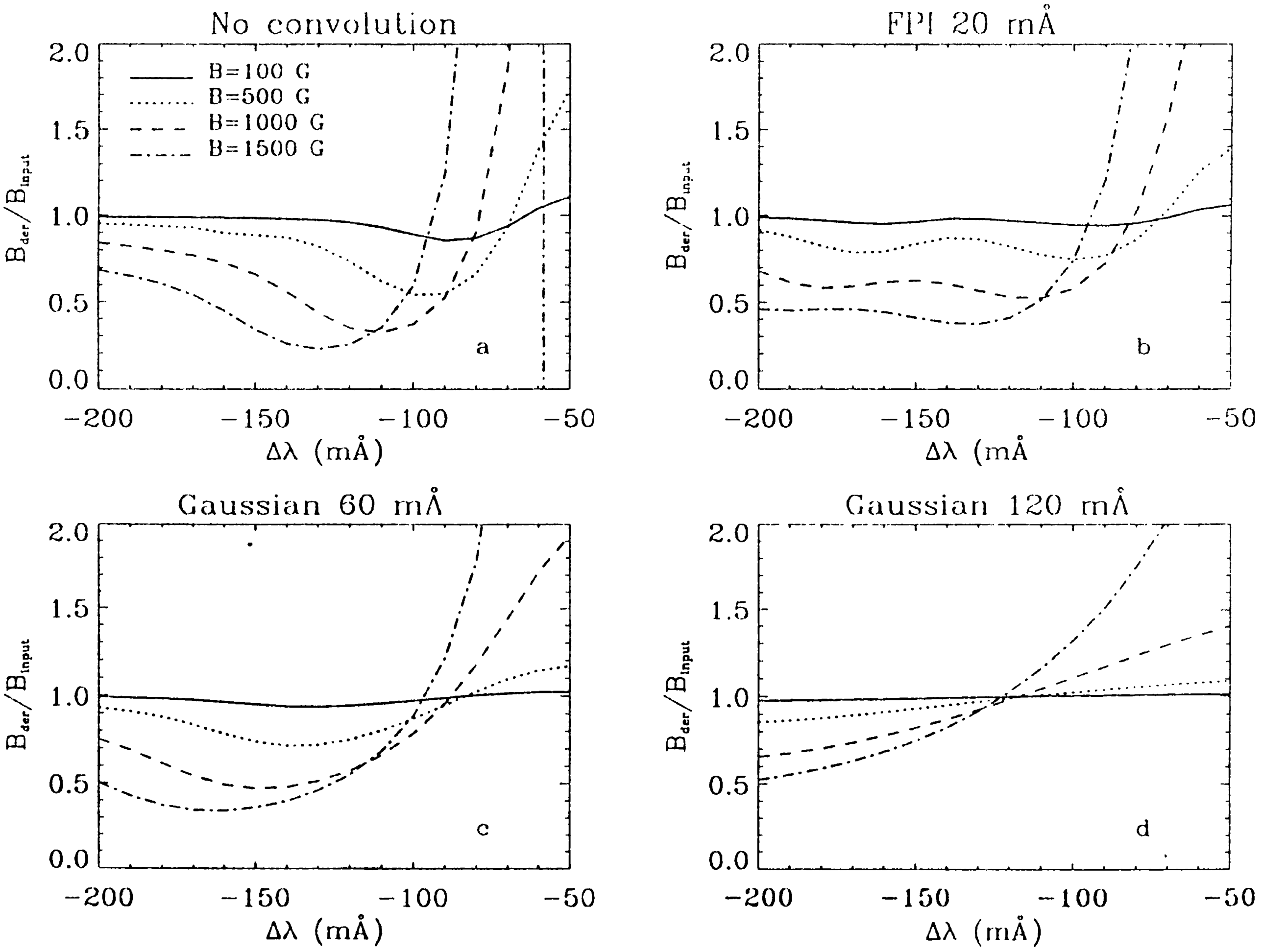

Fig. 7. The derivative method for recovering the magnetic fields. The ratio of the recovered magnetic field to the input magnetic field (for 0° inclination) at different spectral positions, for the various spectral smearing cases. The magnetic fields corresponding to each of the curves are shown on the top left panel.

order to optimize the choice of the spectral line, instrumental profile, and positioning of the filter and to understand the results. For the case of Fe I 5250.2 Å, the method is of practical utility only when using wide instrumental profiles.

3. Instruments and Observations

The observations were carried out at the Vacuum Tower Telescope of NSO/SP, using the tunable Universal Birefringent Filter (UBF) and a tunable Fabry–Pérot interferometer (FPI) (Bonaccini and Stauffer, 1990). The FWHM of the resulting filter is 20 mÅ at 5250 Å. An achromatic quarter-wave plate in front of the UBF, in conjunction with the UBF entrance polaroid, served as the polarization analyzer. The data were recorded using an RCA 504 CCD camera. The angular size of the observed area was about a square arc min, with a pixel size corresponding to 0.25×0.31 arc sec.

Observations of an active region (NOAA 6615) were obtained on May 4, 1991, using the Fe I 5250 Å line. This active region was located near the disc center, at 10° W, 8° N. A correlation tracker (Rimmele *et al.*, 1991) was used to reduce seeing effects during the long (relative to seeing changes) exposure times (∼200 ms). This resulted in a spatial resolution of 0.5 arc sec or better. Each set of measurements consisted of thirteen pairs of monochromatic images of the active region, acquired at equispaced spectral points, each separated by 20 mÅ and covering the interval $\lambda_0 \pm 120$ mÅ, plus a pair of images in the nearby blue continuum. At any given spectral position, each pair consisted of an image taken in right circular polarization $(I+V)$ and another in left circular polarization $(I-V)$, in succession. Each pair of observations took about 2 s, and the entire spectral line scan was completed in less than 50 s. Simultaneous white-light images of the same region were recorded with another CCD camera, at 5000 Å (with a pass-band of 100 Å), using branch feed optics. Figure 8(a) shows a sample white-light image taken during the course of observations. The observed images were corrected for dark current and flat fielding effects. The seeing induced distortions in the monochromatic images were removed using the simultaneous white-light images, via destreching routines (November, 1986).

4. Calibration of the Longitudinal Magnetic Field – Real Data

As seen in Section 2, each calibration method leads to a different estimate of $B_{||}$ when used under different conditions. An optimal choice of wavelengths and instrumental profile is therefore necessary to derive realistic magnetic fields. The results of Section 2 led to the following choice for deriving $B_{||}$ for each of the methods:

(a) Center-of-gravity method: fields obtained using the whole line profile, observed using the narrowest instrumental profile (Airy function, 20 mÅ FWHM).

(b) Calibration at single wavelength, via modeling: fields obtained using the circular polarization at $\lambda_0 - 100$ mÅ, and observed using the widest instrumental profile (Gaussian, 120 mÅ FWHM).

(c) Derivative method in WFA: fields obtained using the circular polarization signal at $\lambda - 100$ mÅ, and observed using the widest instrumental profile.

To simulate instruments with wider profiles than the one used to obtain the data (20 mÅ), we applied appropriate weighted means to the original series of $(I+V)$ and $(I-V)$ images. The possible smearing of polarization signal, due to the non-simultaneity of the images used for the weighted means, is minimized by the stable seeing we had during the observing sequence, by the successive co-registration of the images, and by the short total acquisition time relative to changes in fields.

4.1. THE CENTER-OF-GRAVITY METHOD

The center of gravity of the left $(I-V)$ and right $(I+V)$ circular polarization profiles was derived for all spatial points in FOV, using the thirteen spectral points,

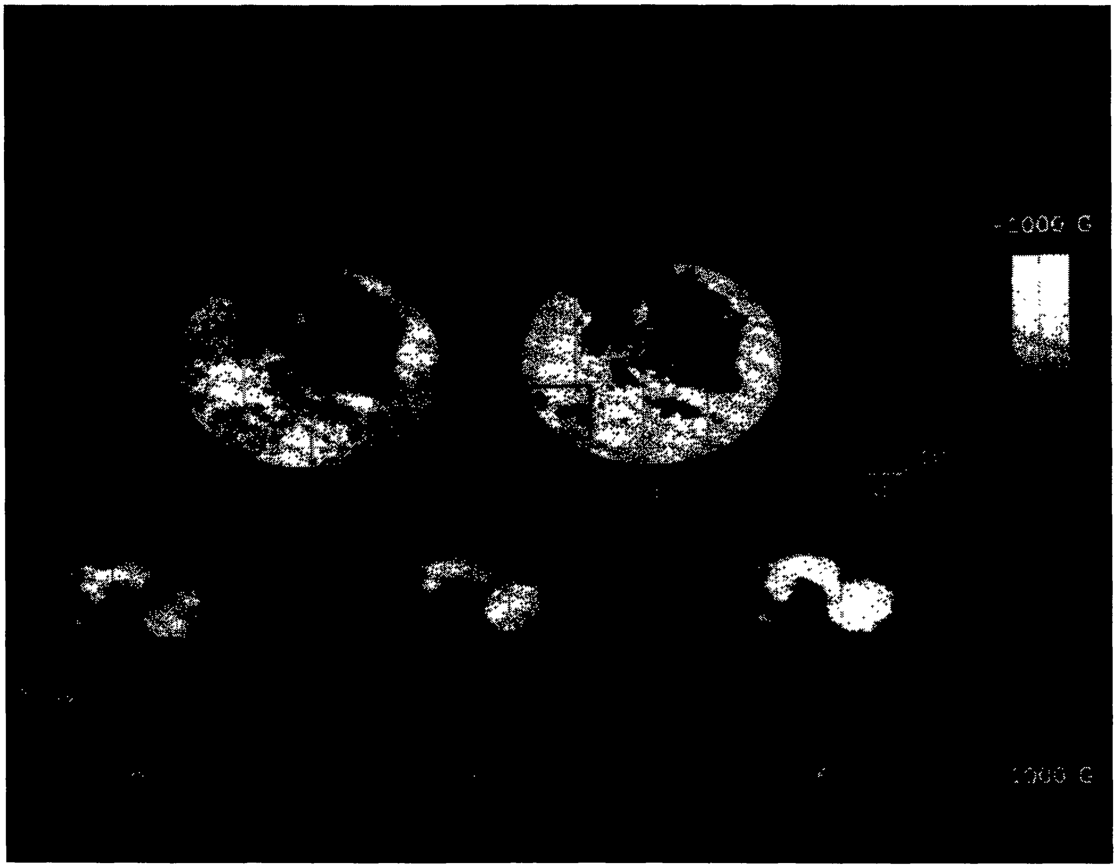

Fig. 8. The longitudinal magnetic fields for active region NOAA 6615, observed on May 5, 1991. (a) Intensity image. (b) The separation of the image into photosphere (brightest area), umbra (darkest area), and penumbra (gray area). The magnetic field derived using the (c) center-of-gravity method, (d) the single-wavelength calibration for a 120 mÅ (FWHM) filter, at −120 mÅ in the blue wing of the line, and (e) the derivative method at −100 mÅ in the blue wing of the line. The image scale and the magnetic field scale are indicated.

for both the original and the spectrally smeared data. The difference in the positions of center-of-gravity of the two orthogonal circular polarization then gives $B_{\|}$ via Equation (2).

As described in Section 2.1, the fact that our observations are limited to $\lambda_0 \pm$ 120 mÅ, introduces an underestimate of the field, that can compromise the validity of any comparison between techniques. Let us denote $B_{\|}(20)$, $B_{\|}(60)$, and $B_{\|}(120)$, respectively, as the magnetic fields derived using spectral resolution of 20 mÅ, 60 mÅ, and 120 mÅ. From the simulated curves of Figure 2(b–d), we find the ratios of the line-of-sight magnetic fields recovered with different spectral resolution. The ratio $B_{\|}(20)/B_{\|}(60)$ varies between 1.0 and 1.05, and the ratio $B_{\|}(20)/B_{\|}(120)$ varies between 1.3 and 1.4. Using the observed data for AR 6615, we have derived the line-of-sight magnetic fields for the different spectral smearing functions. We find that the ratio of the magnetic fields derived with different spectral resolutions compares well. This gives us confidence in the reliability of the $B_{\|}$ values obtained and suggests a possible way to correct the underestimated fields.

Empirically, if we increase $B_{\|}$ obtained with the center of gravity (at the original spectral resolution) by a factor of 1.2 because of the effect of incorrect sampling, the agreement between input values and 'corrected' ones is better than 5% for fields up to 1000 G and at all inclinations. Therefore, if the magnetic fields present in the FOV are not too strong, this simple correction can be applied to our data, giving us a good estimate of the true magnetic fields. Figure 8(c) shows the field obtained for AR 6615, using the center-of-gravity method and the simple correction procedure.

4.2. CALIBRATION AT SINGLE WAVELENGTH THROUGH MODELLING

The fractional circular polarization V/I, at $\lambda = \lambda_0 - 100$ mÅ, was obtained from the data as

$$\frac{V}{I} = \frac{(I+V)_\lambda - (I-V)_\lambda}{(I+V)_\lambda + (I-V)_\lambda} ,$$

where $(I+V)_\lambda$ and $(I-V)_\lambda$ are the corresponding orthogonally polarized images spectrally smeared to mimic the wider (120 mÅ) instrumental profile. The V/I signal was converted into $B_{\|}$ by means of the calibration curves computed in Section 2.2, for both the KM-penumbral and the HSRA-photospheric models.

Figure 8(d) shows the longitudinal field obtained in this way, for AR 6615, using the penumbral model. Although the basic structures present in this field are similar to the one depicted in Figure 8(b), there are at least two clear differences that must be noted. (i) The fields in the spots (positive polarity, Figure 8(d)) are much larger than those depicted in Figure 8(c). (ii) The smaller fields, corresponding to small spatial scale structures in the lower half of the image, are underestimated, in comparison with the center-of-gravity method. The former difference (i) can be explained by a global underestimation, introduced at strong fields by the center-of-gravity method when using an incomplete sample, as discussed in Section 2.1. Another source of error is the inadequacy of the penumbral models to fit the umbral data. The latter difference (ii) is attributed to the fact that small magnetic field elements in the 'quiet' regions of the field of view are underestimated by the penumbral model.

4.3. DERIVATIVE METHOD IN THE WEAK FIELD APPROXIMATION

Using the Stokes' $I \pm V$ signal at $\lambda = \lambda_0 - 100$ mÅ (spectrally smeared by 120 mÅ, as mentioned in Section 4.2 above), we derived the Stokes' V signal, $V = (I+V)_\lambda - (I-V)_\lambda$. The derivative of the I profile was estimated using the difference between the intensity signal at two wavelengths in the blue wing, $\lambda_0 - 80$ mÅ and $\lambda - 120$ mÅ:

$$\Delta I = [(I+V)_{\lambda_0-120} + (I-V)_{\lambda_0-120}] - [(I+V)_{\lambda_0-80} + (I-V)_{\lambda_0-80}] .$$

The line-of-sight magnetic field, $B_{\|}$, was then derived using the relation

$$B_{\|} = -1036 \times V/\Delta I ,$$

where the factor 1036 contains all the constants and atomic parameters for the Fe I 5250.2 line.

Figure 8(e) shows the magnetic field obtained with this method, for AR 6615. Similar differences, as illustrated between Figure 8(c) and 8(d), exist between Figure 8(c) and Figure 8(e). These differences are restricted only to the strong field features within the sunspot. The stronger magnetic field (Figure 8(d)) within the sunspot is intrinsic to the derivative method, which overestimate fields $\geq$800 G (at this wavelength), as illustrated in Figure 7(h). The derivative method would give better results at $\lambda = \lambda_0 - 120$ mÅ, but our data cannot be used to estimate the ΔI factor, at this wavelength.

5. Comparisons

As seen in the previous section, Figure 8 shows a qualitative agreement between the magnetic fields derived with the methods described. In particular, the small spatial scale structures are well recovered with both single and multi-wavelength methods. Thus they are probably real structures and not artifacts. Nevertheless, the fields differ in some aspects, as elucidated data of Section 2. In this section we will try to underline these differences as seen in the real data. For this comparison, we choose the field recovered with the center-of-gravity method, increased by the factor of 1.2 as described in Section 4.2, as the reference. We will refer to this field as the *reference field*.

5.1. $B_{||}$ THROUGH MODELING VERSUS $B_{||}$ CENTER OF GRAVITY

A scatter plot of the $B_{||}$ values obtained with the single wavelength calibration (Section 4.2) versus the reference field is depicted in Figure 9. The total number of points in the scatter plot exceeds 3×10^4. There is a general agreement between the two fields, but the scatter around the one-to-one correspondence is of the order of $\pm$100–120 G, up to a value of 600 G, and larger for fields above this value. This scatter is due to a multitude of factors, as expected in Section 2.2. The reason for overestimating the strong magnetic fields using the single-wavelength method were discussed in Section 4.2.

It is apparent, from Figure 9, that the magnetic field structures within the FOV of the observed active region can be categorized into two major groups, each corresponding to different physical situations. Since one of the major problems in the single wavelength calibration through modeling is the choice of the right model, we present further clarifications of this issue, using our data. We separated the FOV into three regions called *photosphere, penumbra,* and *umbra*, on the basis of their continuum intensity. Given the intensity image, normalized to the mean photospheric intensity, I_0, as shown in Figure 8(a), we have discriminated the *photosphere* as the pixels with an intensity $I > 0.9 I_0$; *penumbra*, as pixels with $0.6 I_0 < I < 0.9 I_0$ and *umbra* as those pixels with $I < 0.6 I_0$. Each of these three groups contained $\sim 2 \times 10^4$, and 10^4 and 3×10^3 pixels, respectively. These three

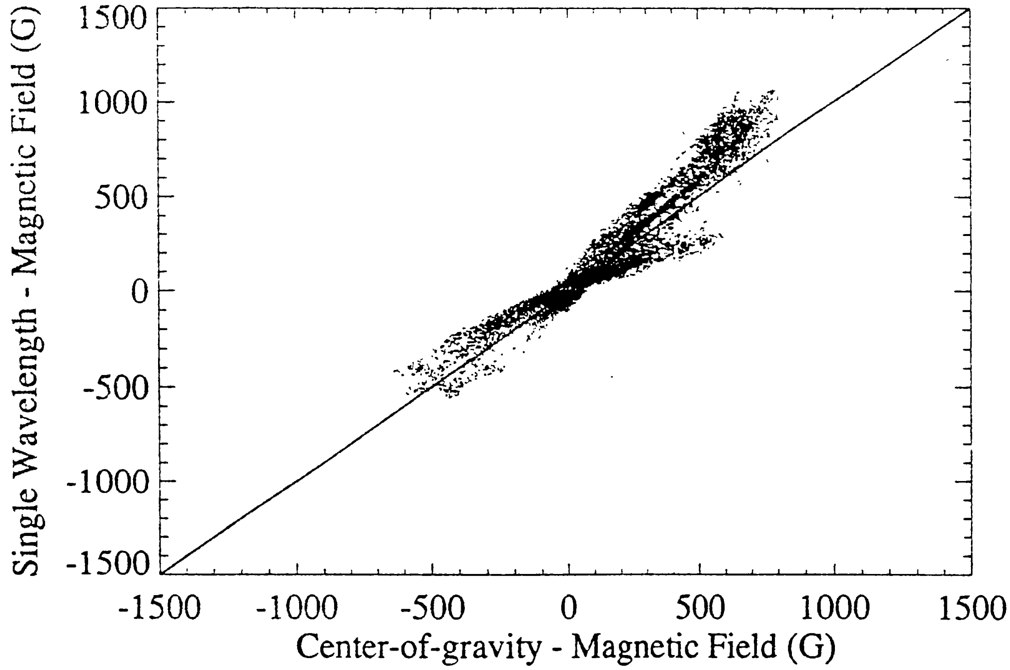

Fig. 9. A scatter of plot of the magnetic fields derived from the single-wavelength versus the magnetic fields derived by the center-of-gravity method. The center-of-gravity magnetic fields have been multiplied by a factor of 1.2 (see text).

different groups are shown as three different shades of gray in Figure 8(b). The darkest shade represents the umbra, the lightest the photosphere, and the middle shade the penumbra.

We show the scatter plots for the magnetic fields from each of these groups compared to the reference field in Figure 10. Two sets of plots are shown, one set obtained using the HSRA-photospheric model and the other set using the KM-penumbral model to calibrate the field. The plots in Figure 10 confirm the results of Section 2.2. When using a penumbral model to calibrate 'photospheric' points, the fields are underestimated by ~15–20% (Figure 10(d)); the opposite is found when 'penumbral' points are calibrated with the photospheric model (Figure 10(b)). For the umbral points (Figures 10(c) and 10(f)), both the photospheric and penumbral models inadequately recover the field. This could be attributed to an inadequate model to describe the umbra, to a saturation of the polarization signal, and to the presence of scattered light in the umbra.

It is also of interest to note a small group of pixels, classified as 'penumbral', but that have a quite different behavior. They appear clearly in Figures 10(b) and 10(e) (near 500 G), sticking out from the main group. Physically, these points are located inside the boxed area, in the lower left half of the FOV (Figures 8(b) and 8(a)), and do not belong to a structured penumbra–umbra system. Similarly, the boxed area in the top of Figure 8(b) has a feature that resembles the photosphere in intensity, but does fit better with a photospheric or penumbral model (Figures 10(a) and 10(d)). These boxed regions do not fit into the definition of umbra, penumbra,

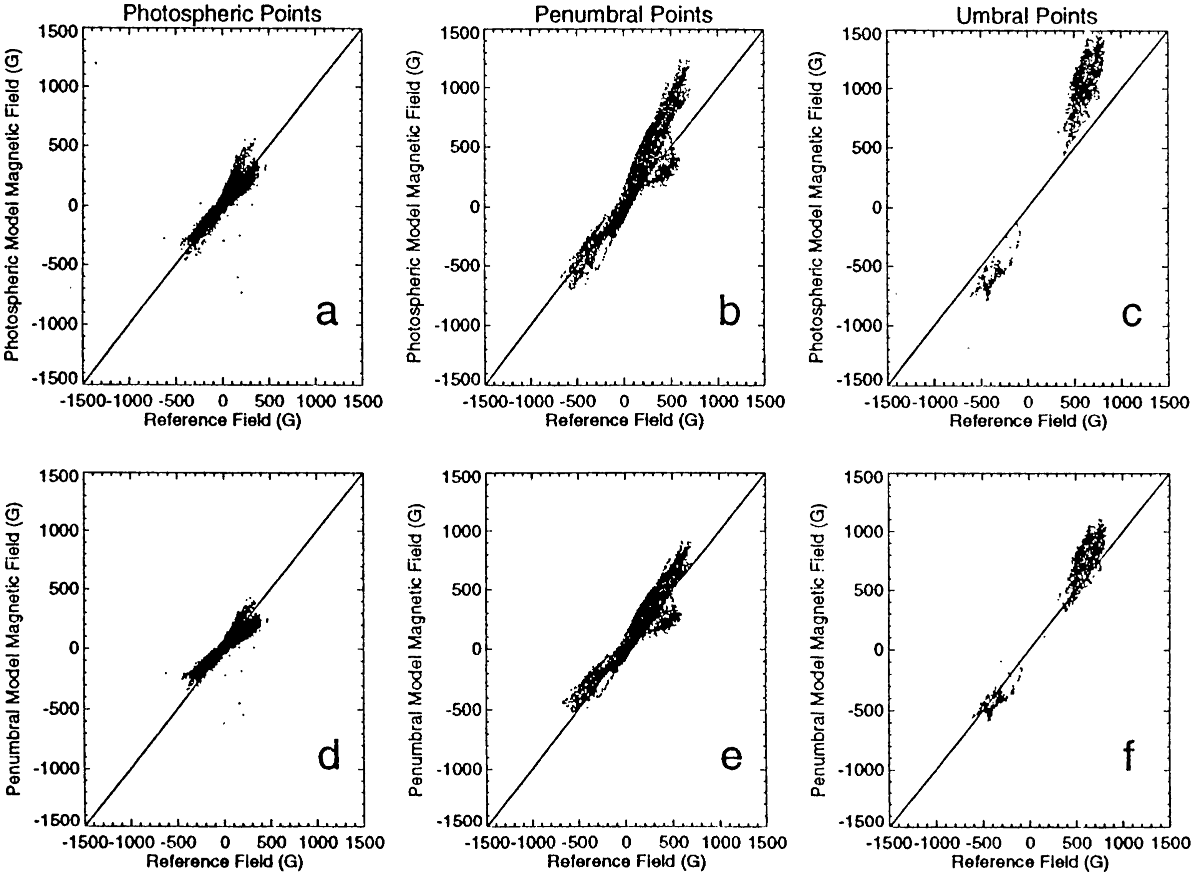

Fig. 10. Scatter plots of the magnetic field derived from the single-wavelength calibration method versus the center-of-gravity method as derived for the photosphere (left panels), penumbra (middle panels), and umbra (right panels). The top row panels are magnetic fields derived using the photospheric model calibration curves. The bottom row panels are magnetic fields derived using the penumbral model calibration curves.

or photosphere, as decided by the models. The boxed region on the bottom left could have a characteristic behavior of pores, rather than a penumbra, and the boxed region on the right could well be a plage. These points are a good example of the difficulties one finds when choosing an atmospheric model to represent the structures under observation.

It may also be worthwhile to note that the measured velocities in the active region were will within the ± 1 km s^{-1} range that was consistent with the assumptions in the calculations. For the single-wavelength calibration, taking velocity effects into account reduced the scatter, when compared with the center-of-gravity method, but not as much as expected from the results of Section 2. This might be due to the fact that velocities were calculated using the entire line profile, while the model-dependent calibration works at only one wavelength.

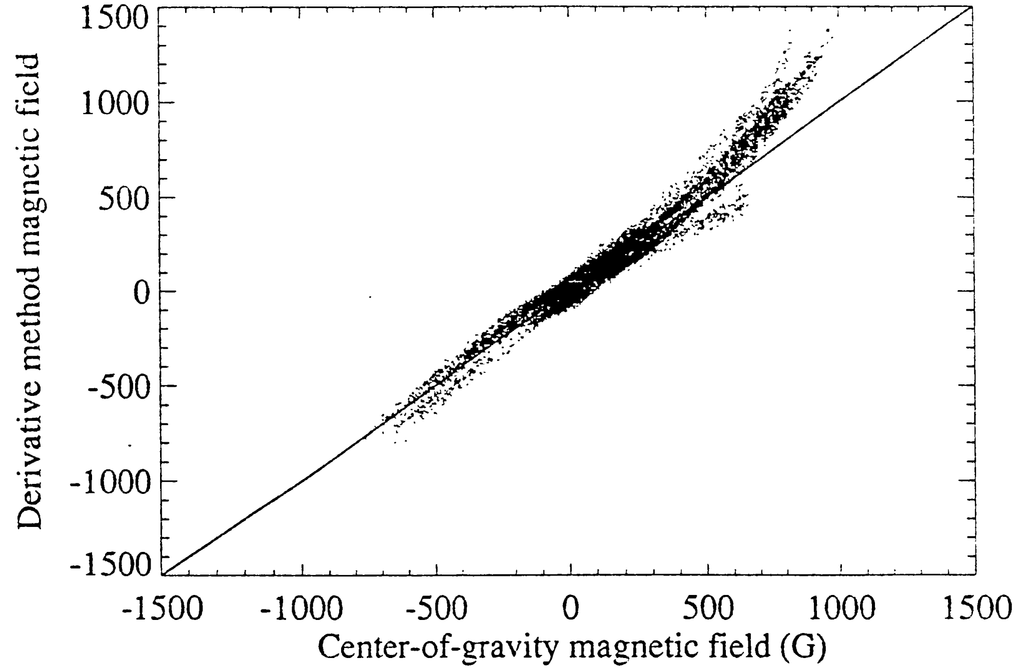

Fig. 11. A scatter plot of the magnetic fields derived from the derivative method versus the magnetic fields inferred by the center-of-gravity method. The center-of-gravity magnetic fields have been multiplied by a factor of 1.2 (see text).

5.2. $B_{\|}$ DERIVATIVE METHOD VERSUS $B_{\|}$ CENTER OF GRAVITY

Figure 11 shows the scatter plot of the field recovered with the derivative method versus the reference field. Within the expected 20% error bar (see Figure 7), we find there is a good agreement between the two fields. For $B_{\|} \geq 1000$ G, there is a rapid growth fo the field on the y-axis, as anticipated in Figure 7. Hence, beyond 1000 G, the derivative method is not suitable for 5250.2 Å line. As mentioned earlier, velocity effects do not play a significant role in the derivative method of calibrating the magnetic field.

6. Summary and Conclusions

Our analysis of the line-of-sight magnetic field calibration methods raises several important questions regarding the calibration of polarization signals acquired with imaging devices at any spectral resolution.

For data at high spectral resolution (FWHM of the instrumental profile $\leq \Delta\lambda_D$), the center-of-gravity method is the only suitable method to recover the longitudinal component of the magnetic field. The derivative method would give acceptable results only in the far wings of the line, where the polarization signal is expected to be below the noise level of available detectors. The calibration at a single wavelength, through modeling, would be heavily influenced by velocity effects. However, to get accurate measures of the magnetic field using the center-of-gravity method, it is necessary to extend the spectral sampling into the far wings. Further tests on our data have revealed that the temporal resultion can be safely improved by sampling with a coarser interval of 40 mÅ at this spectral resolution of 20 mÅ.

For data acquired with lower spectral resolution (FWHM$\geq$2–3$\Delta\lambda_D$), the calibration at single wavelength using models is a fast and reliable method, within 20 –30%. Since the thermodynamic parameters are expected to vary over the FOV, the limitations of this method show up clearly (Section 5.1). Hence, when using high spatial resolution data, the fields recovered with this calibration method might be incorrect with respect to the real physical conditions and velocity effects within the FOV could further complicate the results. A contrasting approach, in the case of low spectral resolution, is by the derivative method, where structural differences and velocity fields are partially accounted for by the use of the local derivative of the Stokes' I profile.

At intermediate spectral resolution, the only method giving acceptable results is the center-of-gravity, if used within a proper spectral interval.

Irrespective of spectral resolution, we find that the single wavelength, model-dependent method and the derivative method yield higher scatter between the recovered and the input magnetic fields. This is due to a combination of factors such as saturation of the Stokes' V signal, velocity effects, inclination effects, the Stokes' V signal having a range of amplitudes for a given magnetic field (recent measurements in the near-infrared region attest to this (Rabin, 1992)), and filling factors. Hence, magnetic fields assigned to different solar features, particularly to intricate features, such as bright and dark penumbral filaments, umbral structures, and plages should be treated with caution. Most magnetographs work at photospheric wavelengths, where it may not be easy to discriminate, for example, a plage while at the disc center. Also, even though we see a range of magnetic field strengths and intensities between the penumbral and umbral structures, we do not have a set of continuous models to represent these variations, particularly at their boundaries. Hence, model-dependent calculations would be prone to some error. In strong field regimes such as umbrae or pores, the polarization signal tends to saturate in the wings of the spectral line, and this in turn restricts the applicability of the model-dependent method.

Simultaneous fitting of the Stokes' I and V profiles, using nonlinear, least-square fitting techniques (Skumanich and Lites, 1987; Balasubramaniam and West, 1991), would offer a better estimate of the magnetic field, but requires a complete line profile measurement. Imaging through a narrow-band filter system at only a few spectral points offers the advantage in speed of acquiring two dimensional maps of the solar magnetic field. This will be adequate for many studies of the evolution of active regions. When using a narrow-band filter system, it is possible to compute correction factors that will permit the recovery of the solar magnetic field with fairly high accuracy in many cases, if the assumption of 100% filling factor is correct.

Although the conclusions of this paper have been arrived at using the Fe I 5250.2 Å line, it is easy to imagine their extension to other Zeeman sensitive lines.

Imaging magnetograph data should be used with caution and due consideration for the many possible sources of error.

Acknowledgements

We gratefully acknowledge support for this work under the AFOSR Project 2311. We thank the Observing Staff at VTT, NSO/Sacramento Peak, for help during the observing run.

References

Ai, G.: 1987, *Publ. Beijing Astron. Obs.* **9**, 27.
Balasubramaniam, K. S.: 1991, *Bull. Am. Astron. Soc* **23**, 1054.
Balasubramaniam, K. S. and West, E. A.: 1991, *Astrophys. J.* **382**, 699.
Bonaccini, D. and Stauffer F.: 1990, *Astron. Astrophys.* **229**, 272.
Cauzzi, G.: 1992, *LEST Technical Report* **56**, 19.
Gingerich, O., Noyes, R. W., Kalkofen, W., and Cuny, Y.: 1971, *Solar Phys.* **18**, 347.
Hagyard, M. J., Gary, G. A., and West, E. A.: 1988, *The SAMEX Vector Magnetograph*, NASA Technical Memorandum 4048, MSFC, Huntsville, Ala.
Hagyard, M. J., Cumings, N. P., West, E. A., and Smith, J. E.: 1982, *Solar Phys.* **80**, 33.
Jefferies, J. T. and Mickey, D. L.: 1991, *Astrophys. J.* **372**, 694.
Jones, H. P., Duvall, T. L., Jr., Harvey, J. W., Mahaffey, C. T., Schwitters, J. D., and Simmons, J. E.: 1992, *Solar Phys.* **138**, 211.
Kjeldseth Moe, O. K.: 1973, *Solar Phys.* **33**, 393.
Kjeldseth Moe, O. and Maltby, P.: 1969, *Solar Phys.* **8**, 275.
Landi Degl'Innocenti, E.: 1976, *Astron. Astrophys. Suppl. Ser.* **25**, 379.
Landi Degl'Innocenti, E.: 1979, *Solar Phys.* **63**, 237.
Landi Degl'Innocenti, E. and Landi Degl'Innocenti M.: 1973, *Solar Phys.* **31**, 299.
Lites, B. W., Elmore, G., Murphy, G., Skumanich, A., Tomczyk, S., and Dunn, R. B.: 1991, in L. J. November (ed.), *Solar Polarimetry*, Proceedings of the 11th NSO Summer Workshop, Sunspot, NM, p. 3.
Lundstedt, H., Johannesson, A., Scharmer, G., Stenflo, J. O., Kusoffsky, U., and Larsson, B.: 1991, *Solar Phys.* **132**, 233.
Makita, M., Hamana, S., and Nishi, K.: 1985, in Mona J. Hagyard (ed.), *Measurements of Solar Vector Magnetic Fields*, NASA Conference Publ., No. 2374, p. 173.
Mickey, D. L.: 1965, *Solar Phys.* **97**, 233.
November, L. J.: 1986, *Applied Optics* **25**, 391.
Rabin, D. M.: 1992, *Astrophys. J.* **391**, 832.
Rees, D. E. and Semel, M. D.: 1979, *Astron. Astrophys.* **74**, 1.
Rimmele, T., Von der Luhe, O., Wiborg, P. H., Widener, A. L., Dunn, R. B., and Spence, G.: 1991, in Mark A. Ealey (ed.), *Active and Adaptive Optical Systems*, SPIE 1542, p. 186.
Rust, D. M. and o'Byrne, J. W.: 1991, in L. J. November (ed.), *Solar Polarimetry*, Proceedings of 11th NSO Summer Workshop, Sunspot, NM, p. 74.
Skumanich, A. and Lites, B. W.: 1987, *Astrophys. J.* **322**, 473.
Stenflo, J. O.: 1989, *Astron. Astrophys. Rev.* **1**, 3.
Title, A. M., Tarbell, T. D., and Topka, K. P.: 1987, *Astrophys. J.* **317**, 892.
Wittmann, A. D.: 1971, *Solar Phys.* **20**, 365.
Zirin, H.: 1985, *Australian J. Phys.* **38**, 961.